

Increasing minority carrier lifetime in as-grown multicrystalline silicon by low temperature internal gettering

M. Al-Amin^{a)} and J. D. Murphy^{b)}

School of Engineering, University of Warwick, Coventry, CV4 7AL, United Kingdom

(Received 1 April 2016; accepted 2 June 2016; published online 17 June 2016)

We report a systematic study into the effects of long low temperature ($\leq 500^\circ\text{C}$) annealing on the lifetime and interstitial iron distributions in as-grown multicrystalline silicon (mc-Si) from different ingot height positions. Samples are characterised in terms of dislocation density, and lifetime and interstitial iron concentration measurements are made at every stage using a temporary room temperature iodine-ethanol surface passivation scheme. Our measurement procedure allows these properties to be monitored during processing in a pseudo *in situ* way. Sufficient annealing at 300°C and 400°C increases lifetime in all cases studied, and annealing at 500°C was only found to improve relatively poor wafers from the top and bottom of the block. We demonstrate that lifetime in poor as-grown wafers can be improved substantially by a low cost process in the absence of any bulk passivation which might result from a dielectric surface film. Substantial improvements are found in bottom wafers, for which annealing at 400°C for 35 h increases lifetime from $5.5\ \mu\text{s}$ to $38.7\ \mu\text{s}$. The lifetime of top wafers is improved from $12.1\ \mu\text{s}$ to $23.8\ \mu\text{s}$ under the same conditions. A correlation between interstitial iron concentration reduction and lifetime improvement is found in these cases. Surprisingly, although the interstitial iron concentration exceeds the expected solubility values, low temperature annealing seems to result in an initial increase in interstitial iron concentration, and any subsequent decay is a complex process driven not only by diffusion of interstitial iron.

© 2016 Author(s). All article content, except where otherwise noted, is licensed under a Creative Commons Attribution (CC BY) license (<http://creativecommons.org/licenses/by/4.0/>).

[<http://dx.doi.org/10.1063/1.4954010>]

I. INTRODUCTION

Multicrystalline silicon (mc-Si) is used in more than half of photovoltaic cells produced currently. Compared to single crystal silicon, it has a lower production cost, but leads to cells with lower efficiencies. One reason for this is that mc-Si contains higher concentrations of defects which act as recombination centres and hence reduce the minority carrier lifetime (henceforth referred to as just “lifetime”). Controlling these defects is key to optimising the efficiency of mc-Si solar cells.

Wafers of mc-Si typically contain a high density of metallic impurities in the form of both point-like defects and precipitates,^{1–3} with impurities originating from the feedstock, crystal growth environment, and also cell processing.⁴ Mc-Si also has structural defects such as grain boundaries and dislocations, which provide low energy sites for the segregation of impurities and for the formation of precipitates.^{5–7} Dislocations in mc-Si are particularly harmful when decorated by metallic impurities.⁸ In cast mc-Si grown by directional solidification, lifetime typically varies significantly with height in the ingot, being highest in the middle and lowest at the top and bottom.^{9,10} The top of the ingot solidifies last and so usually has the highest density of dislocations^{11,12} and has a relatively high impurity content from impurities remaining in the melt.^{13,14} Due to impurity

diffusion from the crucible, the bottom of the ingot^{13,14} and the edges¹⁵ also have relatively high impurity contents. Extrema at the bottom and top of ingots are sometimes referred to as “red zones” when their lifetime is too low for the use in solar cells.

Iron, which is one of the most harmful and ubiquitous impurities, can be present in cast mc-Si in concentrations of 10^{14} to $10^{15}\ \text{cm}^{-3}$.^{14,16} Most of this iron is tied up in a relatively small number of precipitates, and the bulk iron concentration in the form of interstitial iron (Fe_i) or FeB pairs is typically only a small fraction (<1%) of the total.¹⁴ Engineering the distribution of impurities, such as iron, is the key to optimisation of lifetime.¹⁷ Gettering processes are used to redistribute metallic impurities into locations and configurations in which they are less detrimental to lifetime. Extensive research into *external* gettering using near-surface phosphorus, boron or aluminium has been performed (e.g., Refs. 18–21). Targeted external gettering approaches exist for particularly low lifetime wafers, such as saw damage gettering²² and extended gettering based on slower cooling rates.²³ *Internal* gettering, in which impurities are redistributed within the bulk of the material, has also been studied in mc-Si.^{24–27} Internal gettering can occur unintentionally in mc-Si during cooling after high temperature cell processing steps. It can also take place in intentionally designed thermal processes.

Low temperature ($\leq 600^\circ\text{C}$) annealing has been proposed as a way of improving the properties of silicon^{24,26–32} as many of the relevant impurities are sufficiently mobile at

^{a)}m.al-amin@warwick.ac.uk

^{b)}Author to whom correspondence should be addressed. Electronic mail: john.d.murphy@warwick.ac.uk



such temperatures that they can be redistributed. At low temperatures, the solubility of impurities such as iron^{33,34} is low, so there is no need, in principle, to conduct such processes in very clean conditions. Low temperature annealing has empirically been found to improve solar cell efficiency, with Pickett and Buonassisi finding an improvement at 500 °C³⁰ and Rinio *et al.* finding the biggest improvement at 575 °C.^{31,32} The mechanism by which cell efficiencies are improved is not well established, with the improvement likely to be a combined effect of external gettering, internal gettering, and bulk passivation. It is also not known how different parts of the ingot with different defect distributions respond to low temperature processes.

Other researchers have investigated the effects of low temperature annealing at the substrate level.^{24,26,27} In considering the results of these studies, it is vital to consider the details of the experimental conditions used, as we believe these strongly affect the conclusions drawn. Krain *et al.* reported a reduction in interstitial bulk iron concentration by more than one order of magnitude after annealing silicon nitride surface passivated samples at 300 °C to 500 °C.²⁴ The activation energy for the interstitial iron reduction process was similar to that for diffusion of interstitial iron. Krain *et al.* do not report the change in average bulk lifetime, nor do they appear to control the effect of wafer microstructure. It is possible that the low temperature annealing performed in their work was influenced by bulk hydrogenation from the silicon nitride film.^{26,35–37} This can have the effect of passivating bulk defects,³⁸ and it is also possible that hydrogen interacts with iron.^{35,39} Liu and Macdonald have studied internal gettering at 400 °C to 700 °C in samples surface passivated by a high temperature (1000 °C) dry oxidation.²⁶ Although this is likely to have minimised hydrogenation, it will have had the effect of redistributing metallic impurities from their as-grown state. A study by Boulfrad *et al.* reported a lifetime improvement in bottom red zone material by applying annealing at 550 °C after a high temperature pre-annealing step (≥ 950 °C).²⁷ The high temperature pre-treatment will have dissolved metallic precipitates,⁴⁰ and thus, the as-grown state will have also been modified. In summary, whilst low temperature annealing has been shown to have beneficial effects, detailed understanding of its effects on unmodified as-grown mc-Si in isolation from other effects such as bulk hydrogenation is currently lacking.

In this paper, we present results of a systematic set of low temperature annealing experiments on mc-Si wafers sourced from four different height positions of a commercially grown ingot. The samples are first characterised in terms of dislocation density, lifetime, and interstitial iron concentration. Samples are passivated temporarily with an iodine-ethanol (I-E) chemical solution⁴¹ to avoid possible bulk hydrogenation and thermal annealing during passivation. Sister samples from every height position are annealed at low temperatures (300 °C to 500 °C) for a wide range of time periods. At each time step, samples are re-passivated with I-E solution, and the lifetime and interstitial iron distribution are re-measured with photoconductance lifetime measurements and also photoluminescence (PL) imaging. We believe we are therefore able to report accurately the effect of low temperature annealing on

lifetime (as well as interstitial iron concentration), in the absence of added hydrogen, in as-grown mc-Si.

II. EXPERIMENTAL METHODS

A. Sample selection and preparation

Wafers (156 mm × 156 mm) were sourced from four different height positions (top (T), top middle (MT), bottom middle (MB), and bottom (B)) of an edge block from a commercially grown boron doped mc-Si ingot. Neighbouring wafers from all the positions were laser cut into 39 mm × 39 mm samples. The selection of samples used is illustrated by Figure 1. Samples were initially ~200 μm thick, with resistivities in the range of 7.5 Ω cm to 11.5 Ω cm.

Samples were chemically polished with a planar etch solution comprising HF (50%), HNO₃ (69%), and CH₃COOH (100%) in the ratio of 24:58:18 to remove saw damage created by the manufacturer's wafering process. Approximately 30 μm of material was removed from both sides.

B. Iodine-ethanol surface passivation and lifetime characterization

After saw damage removal, samples were subjected to RCA cleaning. Samples were dipped in HF (10%) to remove the native oxide, which is known to degrade the performance of the I-E passivation process substantially,⁴¹ and then were immediately placed in optically transparent sealable plastic bags. A few drops of 0.1 M iodine-ethanol solution was added to each bag at room temperature to form a thin uniform layer on both surfaces. The excess solution and air bubbles were squeezed out prior to sealing.

Lifetime was measured at room temperature by quasi-steady-state photoconductance (QSS-PC)⁴² using a Sinton WCT-120 lifetime tester with a 1.4 cm diameter detection region. In this paper, we use $\tau_{\text{effective}}$ to denote the measured minority carrier lifetime with bulk iron in the FeB state at an injection level of $1 \times 10^{15} \text{ cm}^{-3}$. In order to measure the bulk interstitial iron concentration, [Fe_i], FeB pairs were

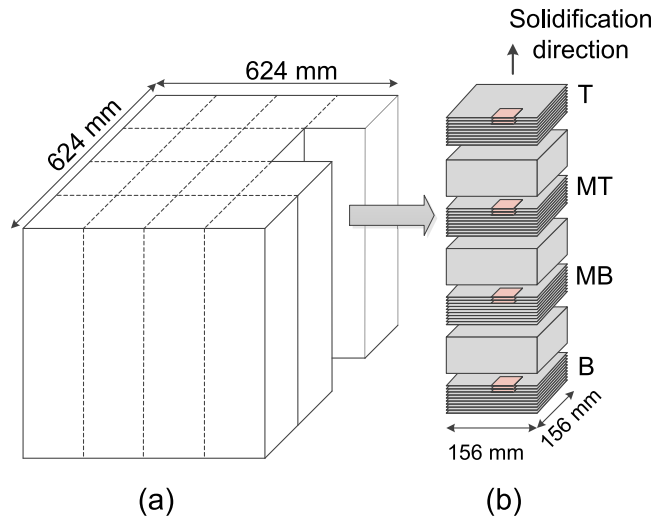


FIG. 1. Illustration showing sample selection from an edge block (b) of a mc-Si ingot (a). Samples (39 mm × 39 mm) (denoted by red squares) were selected from neighbouring wafers from four different height positions: top (T), top middle (MT), bottom middle (MB), and bottom (B).

dissociated by more than 50 consecutive intense flashes (~ 30 suns) of light with a $\sim 10\ \mu\text{s}$ decay constant and final lifetime was measured immediately. The surface passivation was confirmed to be stable under this intense illumination in a control experiment on boron-free *n*-type mc-Si which did not experience significant lifetime changes as a result of the process. To determine $[\text{Fe}_i]$, we use the approach described in detail in Ref. 43, with the Shockley-Read-Hall (SRH) parameters of Rein and Glunz.⁴⁴ The calculation relies on the subtraction of two inverse lifetimes, and it is assumed that other recombination channels are unchanged by the intense illumination. For iron calculations from QSS-PC data, we used an injection level of $\Delta n = 1 \times 10^{15}\ \text{cm}^{-3}$, as this is not at the cross-over point^{44,45} and avoids trapping issues which are prevalent at lower injections.⁴⁶ Lifetime is assumed to be accurate to $\pm 4.3\%$, which is based on the worst within-laboratory standard deviation from an international calibration study published by Blum *et al.*⁴⁷ The uncertainty in interstitial iron concentration is estimated by performing the interstitial iron calculation at the extrema of the lifetime error bars and combining these errors. This means the interstitial iron uncertainty is lifetime dependent. We do not consider systematic errors which may result from errors in the SRH parameters. The detection limit of interstitial iron by the QSS-PC method depends on doping level, injection level, and bulk lifetime due to defects other than Fe_i or FeB (τ_{bulk}). For the most conservative conditions used (lowest τ_{bulk} of $2.2\ \mu\text{s}$), it is estimated around $8.7 \times 10^{11}\ \text{cm}^{-3}$, but it scales approximately linearly with bulk lifetime and can be as low as $1.3 \times 10^{10}\ \text{cm}^{-3}$ for the highest τ_{bulk} of $153\ \mu\text{s}$.

The spatial distribution of lifetime was measured with iron in the FeB and Fe_i states using a BT Imaging LIS-L1 PL imaging system. Excitation is achieved using a light emitting diode (LED) array with emission wavelength of $650\ \text{nm}$ and detection is with a silicon CCD. PL images were calibrated in terms of lifetime by a QSS-PC measurement made at the centre of the same sample.⁴⁸ For the conditions used here, the pixel size is $\sim 160\ \mu\text{m}$. Lifetime measurements were made within a few minutes of initial surface passivation as the quality degrades rapidly. All PL and lifetime images presented in this paper are with iron in the FeB state and were acquired with a $1.1 \times 10^{17}\ \text{cm}^{-2}\text{s}^{-1}$ photon flux with an exposure time of $5\ \text{s}$. After the final measurement, the samples were subjected to a methanol dip followed by RCA cleaning to remove residues of the I-E solution.

The spatial distribution of the interstitial iron concentration was calculated using the model in Ref. 43 based on lifetime changes at every pixel, as reported in Macdonald *et al.*⁴⁹ The injection level used for interstitial iron mapping was lifetime dependent, different for every pixel, and lower than for the QSS-PC calculations to prevent unwanted dissociation of FeB pairs during measurement. The detection limit varies from pixel to pixel and is slightly worse than the QSS-PC interstitial iron measurement because of the lower injection conditions.

C. Low temperature annealing

Three sister samples from every height position were selected for annealing at 300°C , 400°C , and 500°C . RCA

cleaned samples were annealed in a furnace ($60\ \text{cm}$ length, $6.1\ \text{cm}$ diameter) in a fused silica tube under nitrogen ambient. For a given temperature, samples from all height positions were subjected to identical annealing and cooling treatments, as annealing and removal was performed simultaneously. Cooling was always fast, and it is estimated that the samples were at room temperature in $\sim 10\ \text{s}$. After each annealing treatment samples were again subjected to RCA cleaning and were stored in the dark for at least $36\ \text{h}$ to ensure complete re-association of FeB defects.⁵⁰ Samples were then passivated with a freshly-made I-E solution and lifetime was measured as before. A summary of the major processing and characterisation sequences used is shown in Figure 2.

D. Dislocation density measurement

To characterise the structural defect distribution, a sample from each block position was etched. The preferential etch used was HF (50%):CH₃COOH (100%):HNO₃ (69%) in the ratio 36:20:2 (known as the Sopori etch⁵¹). Samples were etched at room temperature for $90\ \text{s}$ with vertical agitation, followed by a dip in a solution of HNO₃ (69%):HF (50%) in a 9:1 ratio. Etched samples were then scanned using an Epson Perfection V-800 Photo Scanner with a resolution of 6400 dots per inch (DPI). Scanned images were calibrated using an optical microscope and the counting algorithm developed by Needleman *et al.*⁵² was used to determine the dislocation distribution.

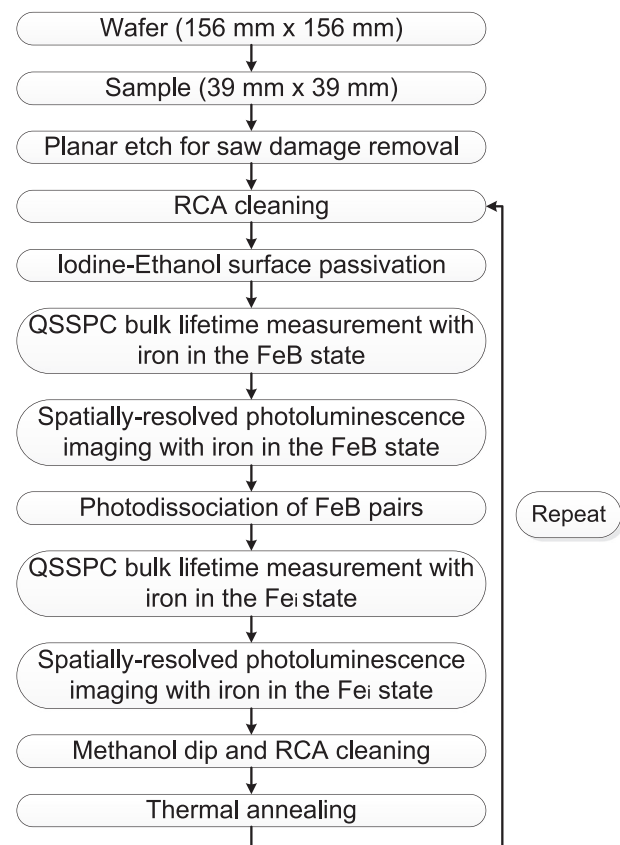


FIG. 2. The processing and characterisation sequence for the low temperature annealing experiments.

III. RESULTS AND ANALYSIS

A. Lifetime and interstitial iron concentrations in as-grown samples

Figure 3(a) shows the distribution of measured bulk lifetime for as-grown samples sourced from the four different height positions. The lifetime varies significantly with position. The average lifetime is lowest in the bottom wafers ($5.6\ \mu\text{s}$) and top wafers ($12.4\ \mu\text{s}$). The bottom middle and top middle wafers have average lifetimes of $44\ \mu\text{s}$ and $28\ \mu\text{s}$, respectively. The distribution of interstitial iron concentration is presented in Figure 3(b). Neighbouring samples at every height position have very similar concentrations. Wafers from the bottom part of the ingot have the highest average concentration ($2.9 \times 10^{12}\ \text{cm}^{-3}$). The average concentrations in the bottom middle ($2.0 \times 10^{11}\ \text{cm}^{-3}$) and top middle ($2.0 \times 10^{11}\ \text{cm}^{-3}$) are substantially lower, and the average concentration at the top is fairly high ($1.0 \times 10^{12}\ \text{cm}^{-3}$).

B. Microstructural characterisation

Figure 4 summarises the microstructural properties of the four different sample types. Figure 4(a) shows scanned optical images of the samples after preferential etching.

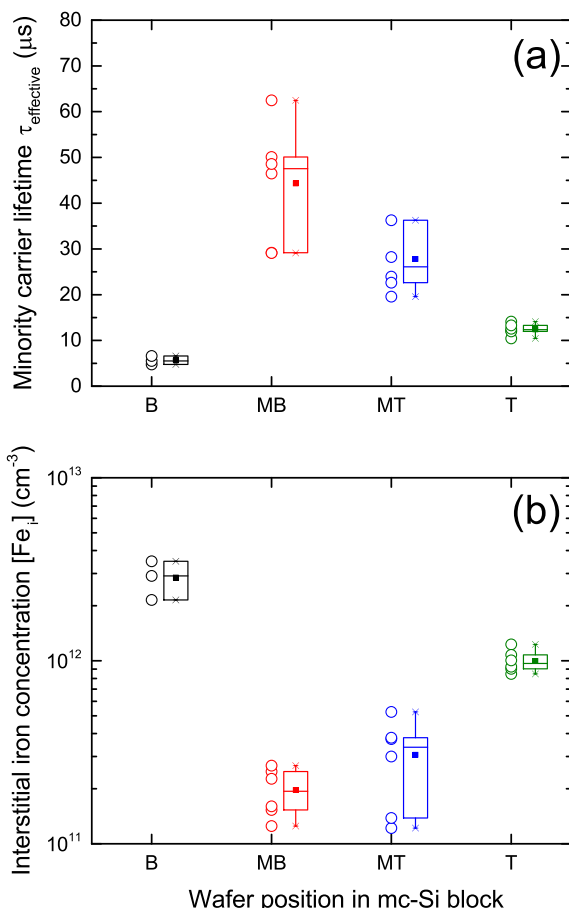


FIG. 3. Distribution of (a) the effective minority carrier lifetime with iron in the FeB state at an injection level of $1 \times 10^{15}\ \text{cm}^{-3}$ and (b) the interstitial iron concentration measured in as-grown samples from different ingot positions. To the right of each data cluster, the open box represents the 25th and 75th percentiles and the median. The solid point within the box is the mean.

These images are analysed using the dislocation counting code⁵² to give the dislocation area density maps in Figure 4(b). The distribution of the dislocation density in these maps is also plotted graphically in Figure 5. The upper limit of dislocation area density is $\sim 2 \times 10^6\ \text{cm}^{-2}$, as around this value dislocation etch pits overlap and are not separable. Furthermore, any other black region in the optical images (e.g. twin boundaries) is presented as regions with very high dislocation density. Figure 4(c) shows PL images of the same samples (prior to the preferential etch) on different scales so adequately to show the microstructural features in samples with substantially different lifetimes. The magnitude of the local PL signal presented in Figure 4(c) is dependent upon the local minority carrier lifetime. The PL images are consistent with the bulk lifetime measurements in Figure 3(a), with the average PL intensity lowest at the bottom of the ingot, highest in the middle, and somewhere in between at the top.

Figure 4(a) shows that samples from different heights of the ingot have clearly different microstructures. Samples from the top have the highest number of etch pits, and relatively few areas with a low dislocation density. Samples from the bottom have relatively fewer etch pits, and relatively more areas with a low dislocation density. The histogram (Figure 5) shows this effect clearly. Samples from the bottom and bottom middle have the most regions with very low ($< 2 \times 10^5\ \text{cm}^{-2}$) dislocation densities, and the frequency distribution falls off with increasing density. Samples from the top and top middle have more even distributions of dislocation densities and have many more regions with high dislocation density than the samples from lower in the ingot. It is noted that a reasonably high frequency of regions with apparently higher dislocation density ($> 2 \times 10^6\ \text{cm}^{-2}$) is observed for all four height positions, and this can be attributed at least partially to how the twin boundaries are analysed by the dislocation counting algorithm as noted above.

The scanned optical images in Figure 4(a) show a reasonably high concentration of twin boundaries in samples extracted from all heights of the ingot. It is interesting to identify twinned regions in Figure 4(a) and inspect the same regions in Figure 4(c). It is clear that the twin boundaries do not substantially affect the PL signal, which means they do not exhibit detectable recombination activity. The recombination activity arises principally in regions with high concentrations of dislocations and from some, but not all, grain boundary types.

C. Bulk low temperature annealing data

Average lifetime data and average interstitial iron concentrations are plotted as a function of annealing time in Figures 6 and 7, respectively. The overall effects are summarised in Table I. The effect of low temperature annealing on both parameters is not straightforward.

The bottom samples exhibit the most intuitive time dependences, with lifetime generally increasing with annealing time and interstitial iron concentration generally falling (although there is a slight initial interstitial iron increase at 400°C and 500°C). Average lifetime in bottom samples was

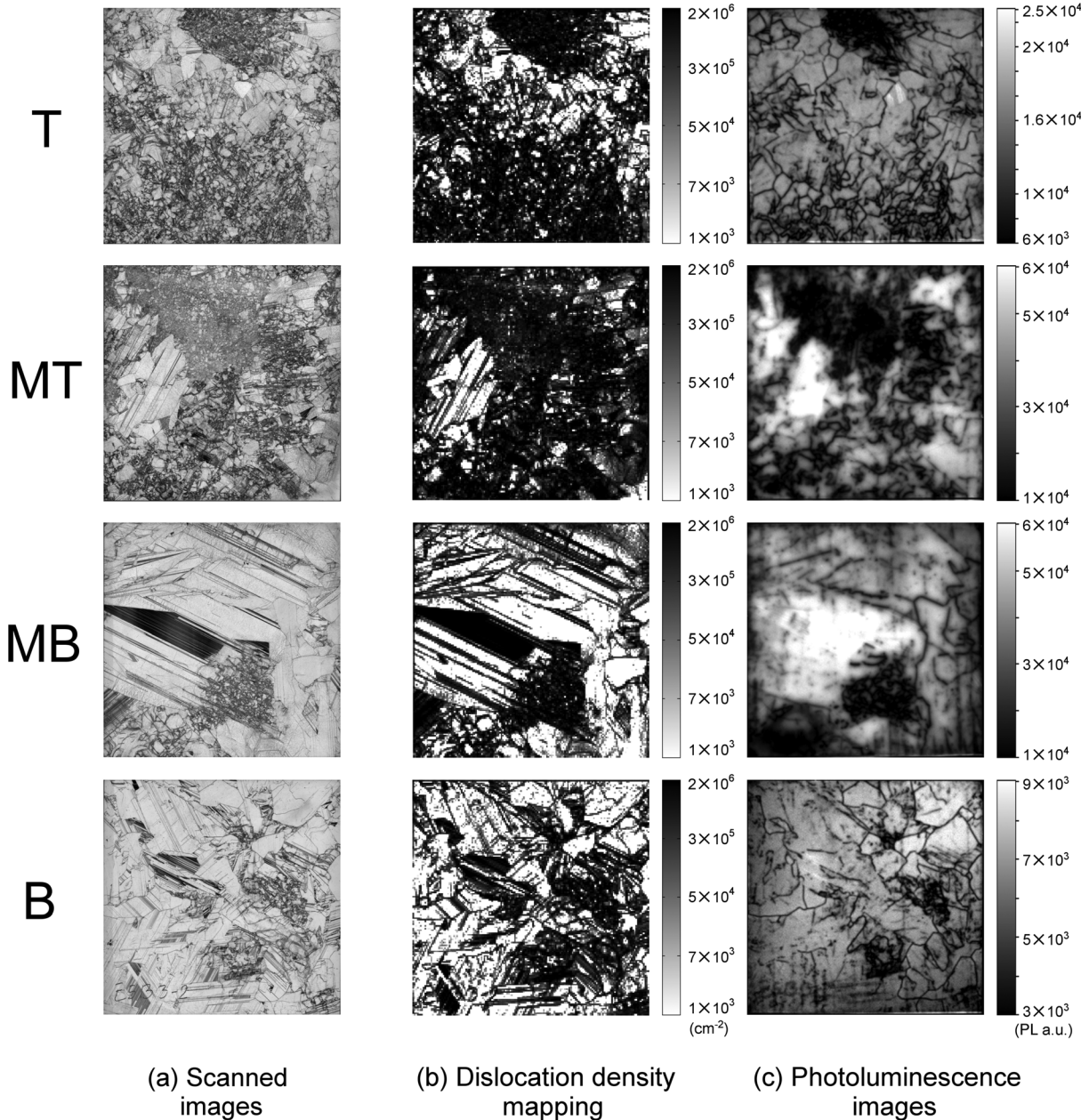


FIG. 4. The first column (a) shows optically scanned images of Sopori etched samples ($39 \text{ mm} \times 39 \text{ mm}$) from the different height positions. The second column (b) show the corresponding dislocation density maps. The third column (c) shows the corresponding PL images of the as-received corresponding samples (before Sopori etching). Different scales are used in (c) to show clearly microstructural features in samples with substantially different lifetimes.

increased at all temperatures investigated. The largest improvement is at 400°C when 35 h of cumulative annealing increases lifetime to ~ 7 times the as-received value. Annealing at 300°C and 500°C gives ultimate improvements of ~ 6 and ~ 4 times. In the best case, lifetime is increased from $5.5 \mu\text{s}$ to $38.7 \mu\text{s}$.

Lifetime in top samples is ultimately improved by annealing at all temperatures considered, although lifetimes initially reduce substantially at 500°C and slightly at 400°C . At 500°C , lifetime in top samples falls from $\sim 12 \mu\text{s}$ to $\sim 2 \mu\text{s}$ within 15 min. This is accompanied by a substantial initial increase in interstitial iron concentration to a peak of $\sim 3 \times 10^{12} \text{ cm}^{-3}$. The initial impact of the annealing appears to be to release interstitial iron into the bulk from somewhere else in the material. It is noted that the two very low ($< 10^{11} \text{ cm}^{-3}$) interstitial iron values for short annealing of

top samples at 500°C plotted in Figure 7 are close to the detection limit and have very large error bars.

Annealing of middle samples (both MT and MB) generally results in an initial lifetime reduction at 500°C , a reduction then improvement at 400°C , and a reduction and slight improvement at 300°C . Interstitial iron concentrations initially increase upon annealing. Given sufficient time, small ultimate lifetime improvements were found at 300°C and 400°C . Annealing at 500°C results in a very abrupt initial reduction in lifetime, similar to that found in top samples.

Interstitial iron measurements were occasionally made on $7 \Omega \text{ cm}$ boron-doped float-zone silicon control samples subjected to the same cleaning and annealing processes as the mc-Si samples. Such control samples did not experience increases in interstitial iron concentration. Figure 7 shows

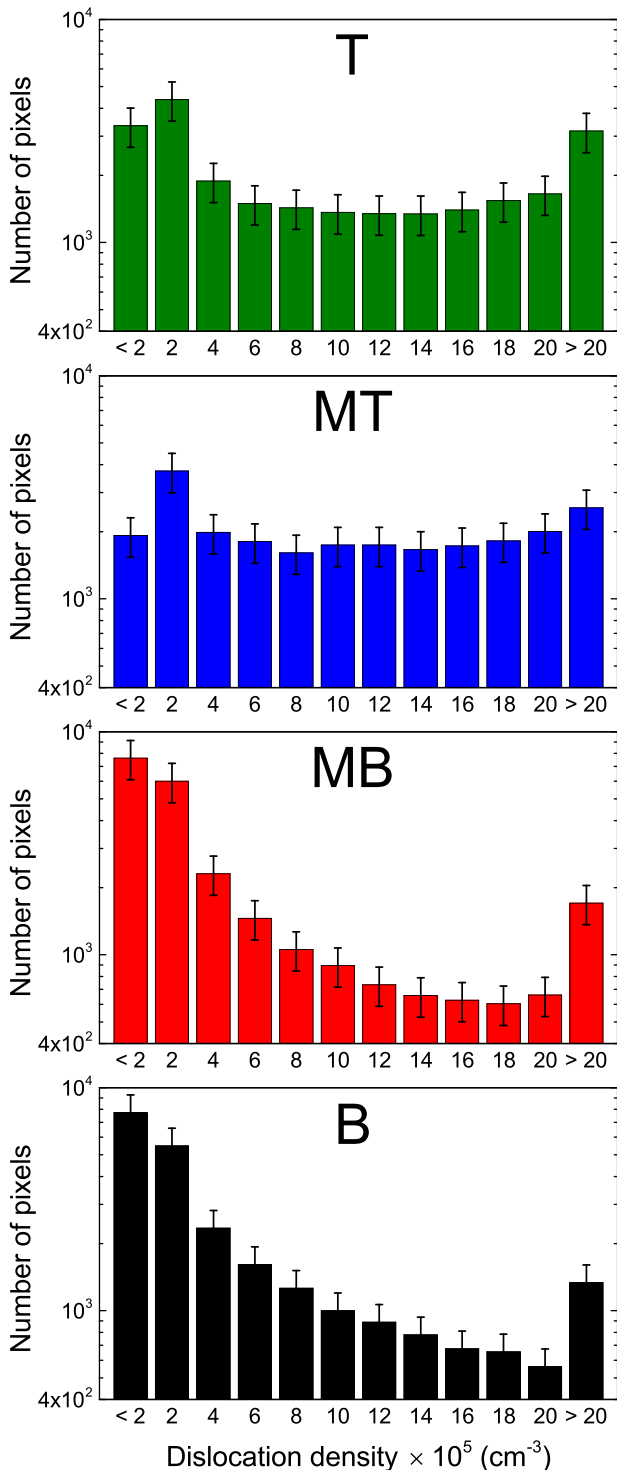


FIG. 5. A frequency distribution of dislocation densities for samples sourced from the four different height positions. A bin width of $2 \times 10^5 \text{ cm}^{-2}$ and 20% error bar are considered in distribution analysis.

the highest interstitial iron concentration measured in mc-Si is $\sim 3 \times 10^{12} \text{ cm}^{-3}$ and that this occurs upon annealing at 500°C for 7.5 h. A float-zone sample annealed under the same conditions had an interstitial iron concentration of $4.4 \times 10^9 \text{ cm}^{-3}$, which is slightly lower than its as-grown concentration of $1.6 \times 10^{10} \text{ cm}^{-3}$. This demonstrates that interstitial iron increases in mc-Si are not from furnace contamination.

D. Spatially resolved low temperature annealing data

Spatially resolved lifetime images were acquired at each processing step for every sample. Lifetime images for three key cases are shown in Figure 8 (Multimedia view), with movies of the lifetime evolution available to download. Figure 8(a) shows the bottom samples annealed at 400°C , Figure 8(b) shows the bottom middle samples annealed at 500°C , and Figure 8(c) shows the top samples annealed at 400°C . It is noted that the values of lifetime plotted are, in general, lower than those from QSS-PC (Figure 6), as the PL imaging conditions used resulted in lower levels of carrier injection and the lifetime is injection-dependent. Figure 9 (Multimedia view) shows maps of the interstitial iron concentration in the same samples and time steps as in Figure 8 with Figure 9(a) showing bottom samples annealed at 400°C , Figure 9(b) bottom middle samples annealed at 500°C , and Figure 9(c) top samples annealed at 400°C . Movies of the evolution of the spatially resolved interstitial iron concentration are also available to download.

In the bottom samples annealed at 400°C (Figure 8(a)), the lifetime is initially low in the bulks of the grains and very low at certain grain boundaries and in the vicinity of dislocation clusters (identified in Figure 4(b)). With increasing cumulative annealing time, the lifetime improves, particularly in the bulks of the grains. Figure 9(a) also shows substantial changes in the interstitial iron distribution which occur during annealing of the same samples. Initially, the interstitial iron concentration is $> 10^{12} \text{ cm}^{-3}$ throughout the wafer, whereas after 35 h of cumulative annealing, it is reduced to be of order 10^{10} cm^{-3} in many regions, with a few regions remaining with higher concentration.

In the bottom middle sample annealed at 500°C , the initial annealing reduces lifetime throughout the wafer (Figure 8(b)). Lifetime then begins to recover in regions where the dislocation density is low (shown in Figure 4(b)). The average lifetime after the last annealing step is lower than the as-grown lifetime. It is notable that the low lifetime regions within the high dislocation-containing areas are much more diffuse (less sharp) after annealing than before. The annealing appears to have caused higher interstitial iron concentrations in regions with high dislocation densities than in the as-grown state (Figure 9(b)). Furthermore, annealing increases recombination associated with certain grain boundary types. Some (but not all) boundary types which exhibited no, or very little, detectable recombination contrast in the as-grown state exhibit stronger recombination contrast.

The lifetime in a top sample annealed for 1 h at 400°C has decreased slightly, but it recovers and improves with further annealing (Figure 8(c)). The initial decrease in lifetime after 1 h appears to be due to a lowering of lifetime in the bulk of the grains. This does not correlate with the interstitial iron map (Figure 9(c)) which shows the interstitial iron concentration to fall in most parts of the material.

E. Correlation of bulk lifetime and iron changes

The correlation between lifetime change and interstitial iron concentration change may provide evidence for the origin of the lifetime change. At each cumulative annealing

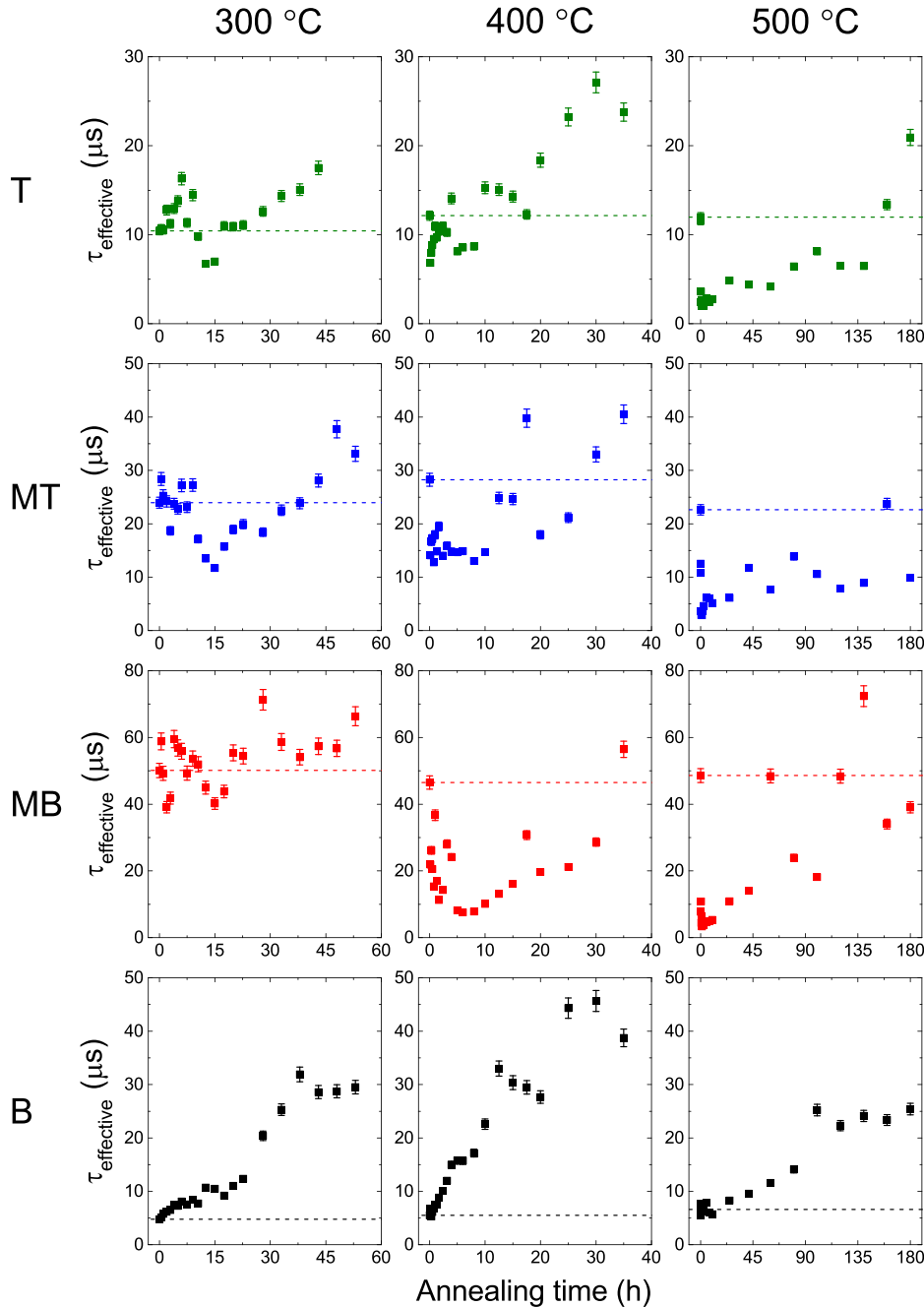


FIG. 6. Effective minority carrier lifetime with iron in the FeB state ($\tau_{\text{effective}}$) measured by QSS-PC at an injection level of $1 \times 10^{15} \text{ cm}^{-3}$ for samples from the top (T), top middle (MT), bottom middle (MB), and bottom (B) of the mc-Si ingot. Sister samples were annealed at 300°C , 400°C and 500°C for the cumulative annealing time plotted. The dashed lines represent the as-grown values.

time, t , we have the lifetime, $\tau_{\text{effective}}(t)$, and the interstitial iron concentration, $[\text{Fe}_i](t)$. We also have the as-grown lifetime before any annealing, $\tau_{\text{effective}}(0)$, as well as the as-grown interstitial iron concentration $[\text{Fe}_i](0)$. If the lifetime changes occur solely due to changes in interstitial iron concentrations, we might expect the change in normalized recombination rate to correlate with the change in normalized interstitial iron concentration according to

$$\frac{\frac{1}{\tau_{\text{effective}}(t)} - \frac{1}{\tau_{\text{effective}}(0)}}{\frac{1}{\tau_{\text{effective}}(0)}} = A \left(\frac{[\text{Fe}_i](t) - [\text{Fe}_i](0)}{[\text{Fe}_i](0)} \right) \quad (1)$$

where A is a proportionality function.

Figure 10 shows plots for the different block heights in accordance with Equation (1). The diagonal dashed lines

represent 1:1 correlation between the normalized recombination rate change and the normalized interstitial iron concentration change. Figure 10 shows a good 1:1 correlation for samples from the bottom of the ingot annealed at the three different temperatures. For the top samples, there is a reasonably good relationship at 300°C and 400°C , but a fairly poor relationship at 500°C . Samples from the middle part of the ingot have a weak relationship at 300°C and 400°C temperatures and a very weak relationship at 500°C .

IV. DISCUSSION

A. Characterisation of as-grown samples

Characterisation of the as-grown samples shows they are typical of cast mc-Si. Figure 3(a) shows the average lifetime distribution, which is qualitatively consistent with

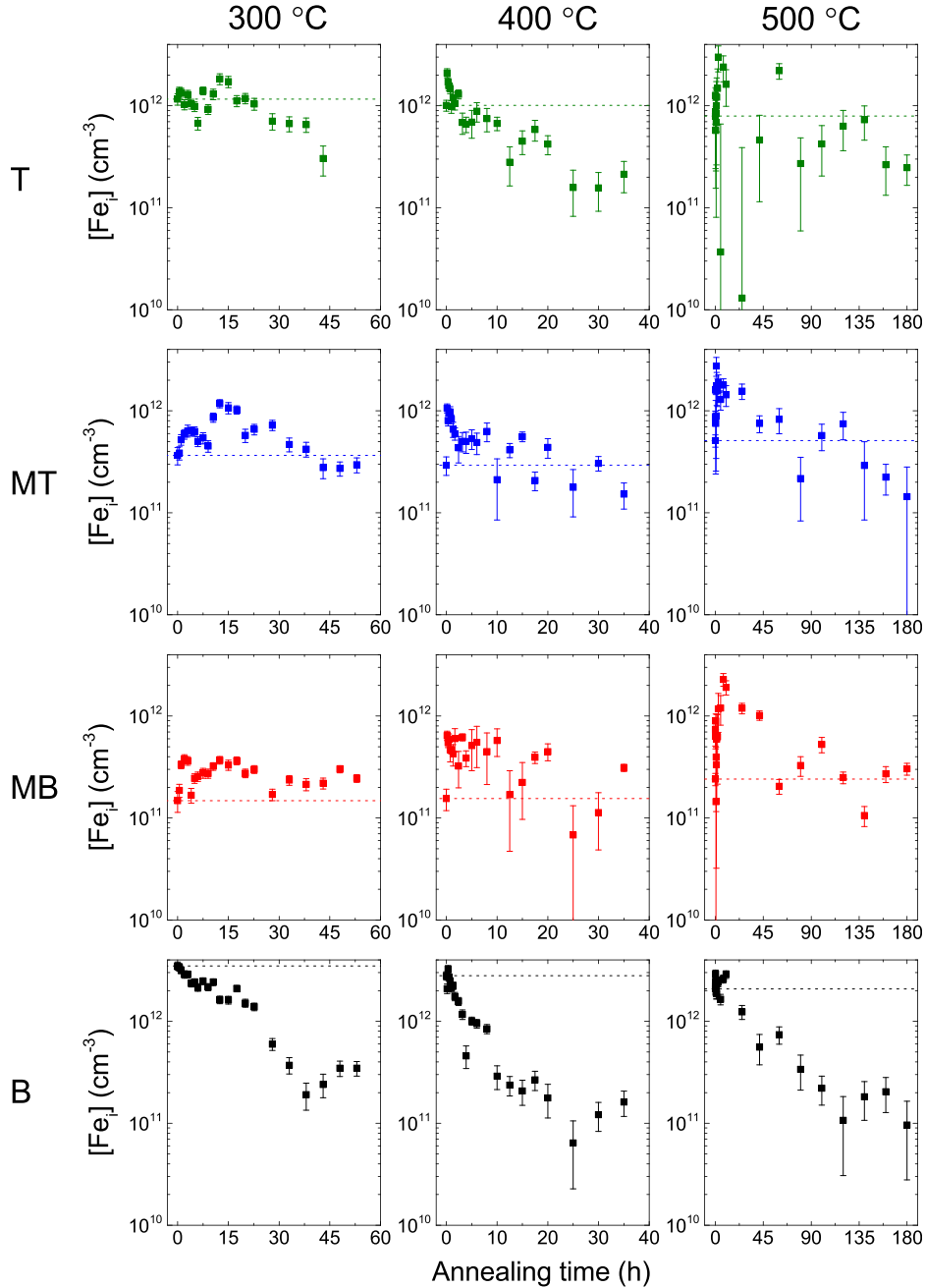


FIG. 7. Interstitial iron concentration ($[Fe_i]$) from QSS-PC measurements for samples from the top (T), top middle (MT), bottom middle (MB), and bottom (B) of the ingot. Sister samples were annealed at 300 °C, 400 °C, and 500 °C for the cumulative annealing time plotted. The dashed lines represent the as-grown values.

other studies.^{9,10} The trend is well understood. The increase towards the top of the ingot is because it is last to solidify and the low segregation coefficient of iron means the melt's iron concentration increases with time.¹⁴ The high value at the bottom of the ingot is due to in-diffusion from the crucible.¹³

Figures 4(a) and 4(b) show that the microstructures of the samples vary with ingot position. The histogram (Figure 5) shows that there are more regions of high dislocation density in the top and top middle of the block than at the bottom or the middle bottom. These observations are consistent with those of Ryningen *et al.*¹² who trace dislocation clusters from the top of the block downwards, and those of Stokkan who found an increase in dislocation density towards the top of the ingot.¹¹ The regions of high dislocation density generally give rise to lower PL signals and have lower carrier

lifetime than low dislocation density regions, as shown in Figure 4(c) and the as-grown lifetime maps in Figure 8. This is as expected from many previous studies (e.g. Ref. 53). The lack of recombination at twin boundaries is consistent with other reports which show them to have very low (or perhaps no) recombination activity.^{11,54,55}

Although the bottom of the wafer has a relatively low density of dislocations, it has the lowest starting carrier lifetime of any of the regions investigated (Figure 3(a)). This is at least partially due to the relatively high concentration of interstitial iron which acts as a recombination centre in the bulk (Figure 3(b)) and the as-grown images in Figure 9). Lifetime in wafers with relatively high concentrations of interstitial iron is likely to be affected by low temperature annealing at 300 °C to 500 °C as interstitial iron diffuses fairly rapidly at these temperatures.⁵⁶

TABLE I. Summary of starting and final effective lifetimes (with iron in the FeB state) and interstitial iron concentration, and their relative values after the final annealing stage.

Ingot position	Annealing temperature (°C)	Total annealing time (h)	As-grown		After longest time annealing		Improvement in bulk lifetime $\frac{\tau_{\text{effective}}(t_{\max})}{\tau_{\text{effective}}(0)}$	Reduction in iron concentration $\frac{[\text{Fe}_i](0)}{[\text{Fe}_i](t_{\max})}$
			$\tau_{\text{effective}}(0)$ (μs)	$[\text{Fe}_i](0)$ ($\times 10^{11} \text{ cm}^{-3}$)	$\tau_{\text{effective}}(t_{\max})$ (μs)	$[\text{Fe}_i](t_{\max})$ ($\times 10^{11} \text{ cm}^{-3}$)		
T	300	43	10.4	11.6	17.5	3.0	1.7	3.8
	400	35	12.1	10.1	23.8	2.1	2.0	4.8
	500	180	12.0	7.9	20.9	2.5	1.8	3.2
MT	300	53	24.0	3.7	33.1	3.0	1.4	1.2
	400	35	28.2	2.9	40.5	1.5	1.4	1.9
	500	180	22.6	5.1	9.86	1.4	0.44	3.5
MB	300	53	50.1	1.5	66.4	2.5	1.3	0.60
	400	35	46.5	1.6	56.4	3.1	1.2	0.50
	500	180	48.6	2.4	39.1	3.0	0.80	0.79
B	300	53	4.76	35.0	29.5	3.5	6.2	10.1
	400	35	5.52	28.0	38.7	1.6	7.0	17.3
	500	180	6.61	20.8	25.4	0.96	3.8	21.6

B. Interstitial iron increases upon annealing

One of the most surprising findings is that low temperature annealing causes an initial increase in the interstitial iron concentration (Figure 7). This is surprising because the levels of interstitial iron are supersaturated,^{33,34,56} and hence, there is a driving force for iron to come out of solid solution, rather than to enter it. Such an increase did not appear to be observed by Krain *et al.*,²⁴ nor Liu and Macdonald.²⁶ Iron “bleeding” from iron silicide precipitates in mc-Si is a well-known phenomenon at processing temperatures $\geq 800^\circ\text{C}$,^{57,58} and is explained by the increased solid solubility of interstitial iron relative to iron silicide at high temperatures causing the bulk concentration of the interstitial iron to increase. Low temperature solubility data are not available, but extrapolation of high temperature solubility data for $\geq 800^\circ\text{C}$ ⁵⁶ gives $\sim 2 \times 10^7 \text{ cm}^{-3}$ at 500°C , and extrapolation of medium temperature solubility data at 600°C to 800°C ^{33,34} gives $\sim 2 \times 10^9 \text{ cm}^{-3}$ at 500°C . The interstitial iron concentration in our samples increases to $\sim 3 \times 10^{12} \text{ cm}^{-3}$ at 500°C , which is at least three (and possibly more than five) orders of magnitude higher than extrapolated solubility trends.

Analysis of the interstitial iron release is most feasible in bottom middle samples, because of their relatively low as-grown concentrations. Peak concentrations of $3.8 \times 10^{11} \text{ cm}^{-3}$ at 300°C , $6.4 \times 10^{11} \text{ cm}^{-3}$ at 400°C , and $2.3 \times 10^{12} \text{ cm}^{-3}$ at 500°C were measured (Figure 7). The temperature dependence suggests the involvement of a solubility driven process with respect to a different iron-containing phase or state within the material than for the higher temperature solubility data (the float-zone control samples rule out the possibility of furnace contamination). As annealing continues, the interstitial iron released is then transformed into a state which is not interstitial iron.

C. Effect of low temperature annealing

Our time-consuming methodology which relies on re-passivation at each processing stage and annealing without surface passivation in place enables us to report bulk

lifetime values which are not influenced by hydrogenation or changes in surface passivation quality. Previous low temperature annealing studies tend to report interstitial iron concentration,^{24,30} cell efficiency,^{30,31} or lifetimes after high temperature processing.^{26,27} Whilst these all suggest beneficial effects in certain circumstances, until this study there are very few available data on just the thermal effect of low temperature annealing on lifetime in as-grown mc-Si.

In bottom wafers, Figure 10 shows a good correlation between the normalized change in recombination rate (reciprocal lifetime) and the normalized change in interstitial iron concentration. This means that the lifetime change in bottom wafers can be explained mainly by the removal of interstitial iron from the bulk. The evolution of the spatial distribution of interstitial iron is broadly similar to the observations of Liu and Macdonald.²⁶ The absence of any external gettering layer means it is likely that interstitial iron is gettered to internal features, such as iron-containing precipitates, grain boundaries, and dislocations. The kinetics does not exclude the possibility of interstitial iron gettering to the samples’ surfaces, although previous work in single crystal silicon suggests this is unlikely.³⁴

The effect of low temperature annealing on top wafers is more complex than for bottom wafers. Although lifetime is ultimately increased for all temperatures used, the magnitude of the improvement and also the final lifetime is less favourable (Figure 6 and Table I). Figure 8(c) shows that after 1 h at 400°C the lifetime decreases slightly, but this does not correlate with the corresponding interstitial iron map in Figure 9(c) in which the interstitial iron concentration falls in most regions. This suggests that reconfiguration of a defect other than interstitial iron is responsible for the initial lifetime reduction. With the exception of this initial effect, for top samples annealed at 300°C and 400°C , there is a reasonably good correlation between lifetime change and interstitial iron change (Figure 10), as was found in bottom samples. The lifetime changes in top samples at 500°C do not, in general, correlate with the interstitial iron changes in a simple way. This could mean that another impurity is

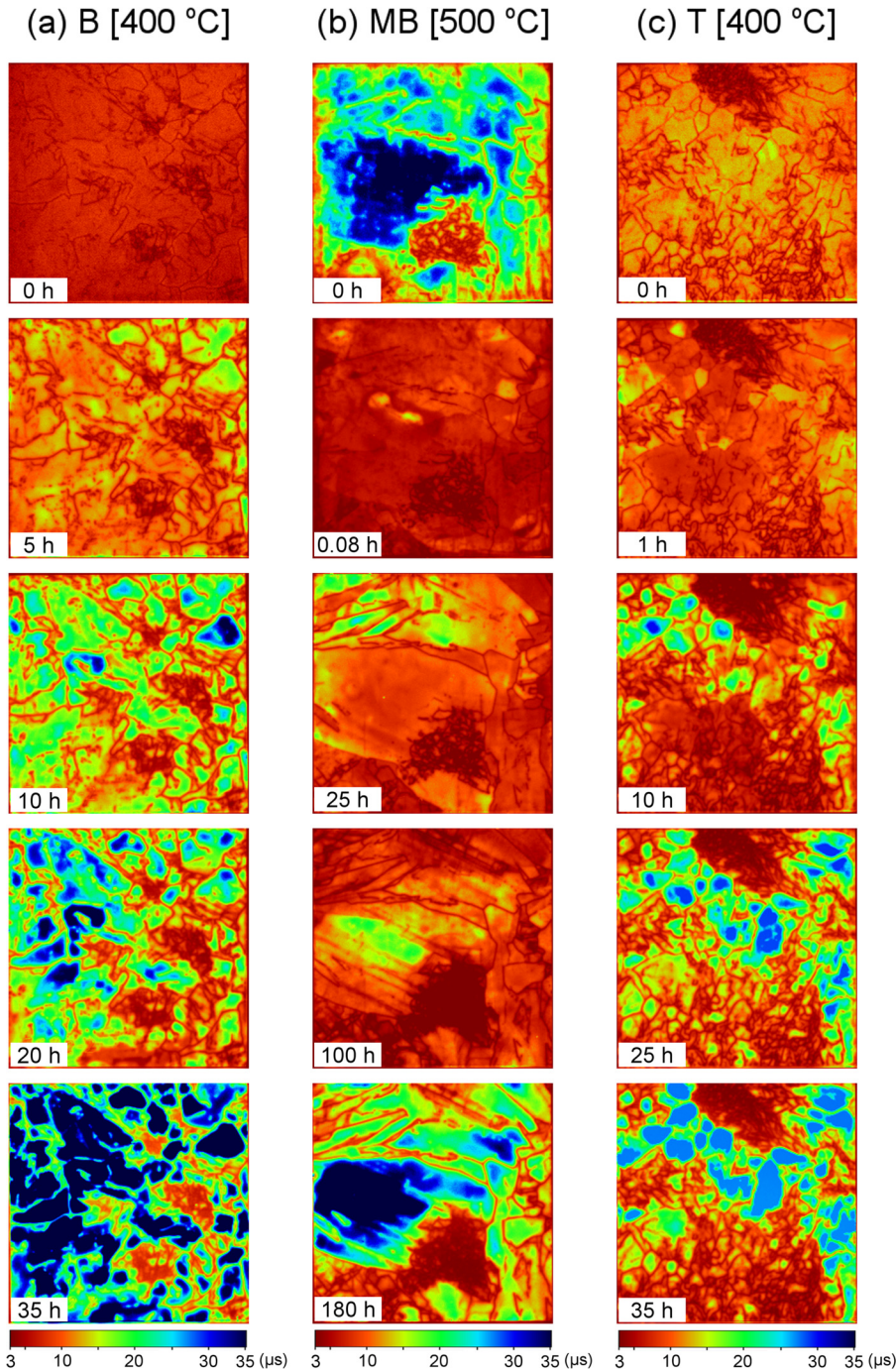


FIG. 8. Spatial distribution of minority carrier lifetime with iron in the FeB state in selected samples (39 mm × 39 mm). Figure 8(a) shows a bottom (B) sample annealed at 400 °C. Figure 8(b) shows a bottom middle sample annealed at 500 °C. Figure 8(c) shows a top sample annealed at 400 °C. The injection levels are lifetime-dependent in the range $6.1 \times 10^{12} \text{ cm}^{-3}$ to $4.0 \times 10^{14} \text{ cm}^{-3}$ (mean: $1.0 \times 10^{14} \text{ cm}^{-3}$). (Multimedia view) [URL: <http://dx.doi.org/10.1063/1.4954010.1>] [URL: <http://dx.doi.org/10.1063/1.4954010.2>] [URL: <http://dx.doi.org/10.1063/1.4954010.3>]

involved at this temperature, or that iron is present in a different state.

Also for top samples, it is instructive to compare the lifetime maps in Figure 8(c) with the top dislocation density map in Figure 4(b). Parts of the sample with relatively low dislocation densities undergo a much larger lifetime improvement upon annealing than those with higher densities. The regions with very high dislocation densities are found to get slightly worse after annealing. This shows that impurities, including interstitial iron, are internally gettered to regions with high dislocation densities. This is to be expected as dislocations provide low energy sites for the segregation of impurities such as iron⁶ and similar results are found after phosphorus diffusion gettering at higher

temperatures.⁵³ Differences in response between top and bottom wafers is probably therefore due to their different microstructures, with top wafers having a higher average dislocation density than the bottom wafers. As suggested by Boulfrad *et al.*²⁷ it could also be the case that the higher oxygen concentration in the bottom wafers due to the segregation coefficient being greater than unity causes oxide precipitates to form upon low temperature annealing and act as trapping sites for iron,^{59,60} although given the absence of a high temperature oxide precipitate growth stage in our work we favour an explanation involving dislocations.

For middle samples, low temperature annealing as performed here (without possible bulk hydrogenation) at best results in marginal improvements; at worst the lifetime

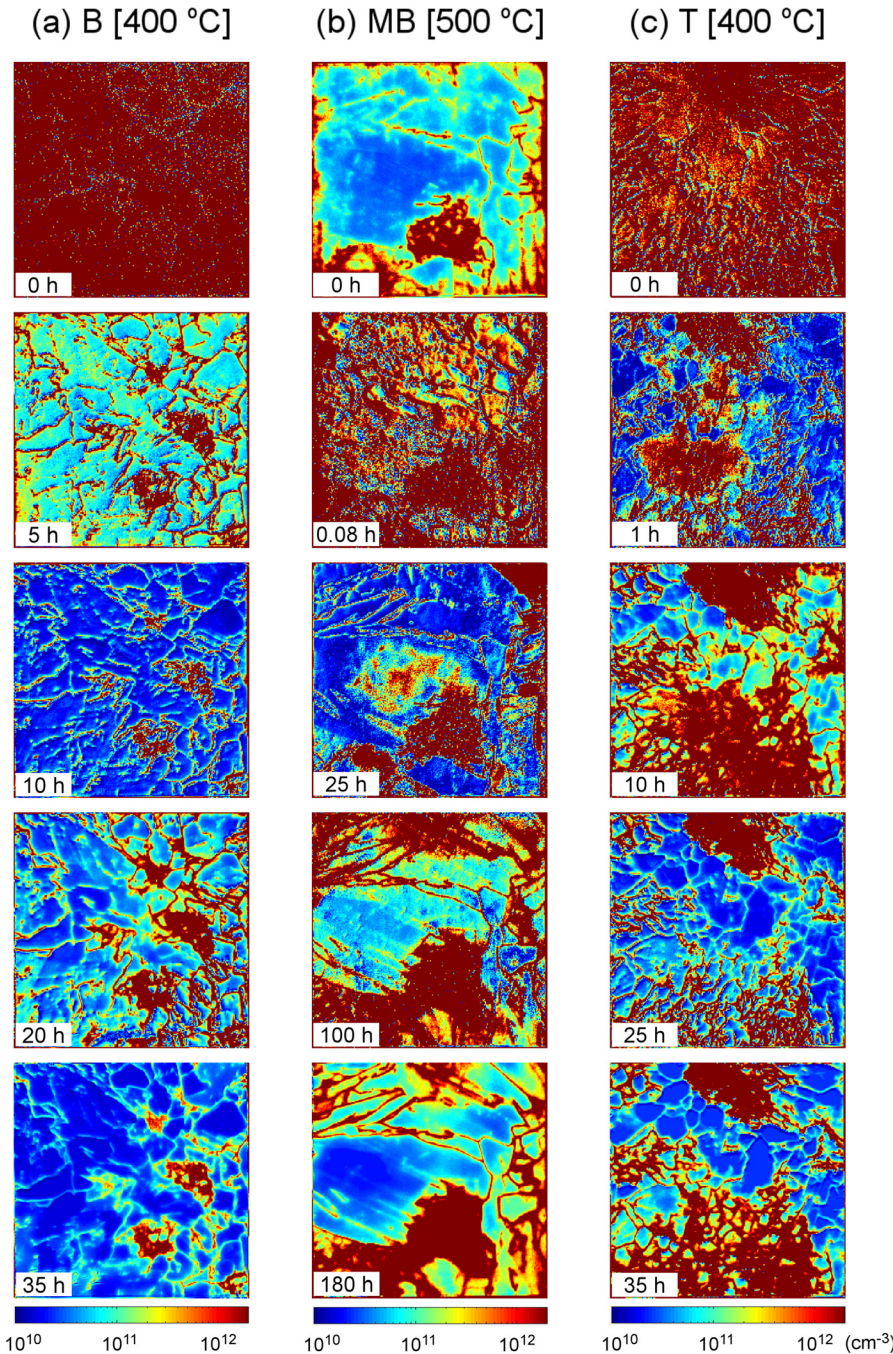


FIG. 9. Spatial distribution of interstitial iron concentration in mc-Si samples ($39\text{ mm} \times 39\text{ mm}$) for the same samples shown in Figure 8. Figure 9(a) shows a bottom (B) sample annealed at 400°C . Figure 9(b) shows a bottom middle sample annealed at 500°C . Figure 9(c) shows a top sample annealed at 400°C . The injection levels in the lifetime images used to create the $[\text{Fe}_i]$ images ranged from $2.8 \times 10^{12}\text{ cm}^{-3}$ to $6.9 \times 10^{14}\text{ cm}^{-3}$ (mean: $1.2 \times 10^{14}\text{ cm}^{-3}$). (Multimedia view) [URL: <http://dx.doi.org/10.1063/1.4954010.4>][URL: <http://dx.doi.org/10.1063/1.4954010.5>][URL: <http://dx.doi.org/10.1063/1.4954010.6>]

is reduced substantially if the samples are not annealed for sufficient time. Lifetime changes which occur in middle samples do not correlate in a simple way with the change in interstitial iron concentration (Figure 10). The correlation is particularly poor at 500°C . Although annealing at 500°C does affect the interstitial iron concentration (Figure 7), we conclude that annealing at this temperature must also affect the concentration of another defect or other defects and it is unclear whether substantial stable improvements are ever realised at 500°C . Defects other than interstitial iron also have an effect at 300°C and 400°C although the effect is smaller. The spatially resolved lifetime maps for bottom middle samples at 500°C (Figure 8(b)) show much greater contrast at certain grain boundaries after annealing. This is presumably because they have getterted impurities from the

bulk. This observation is consistent with electron beam induced current (EBIC) studies of Chen *et al.*, which found increased EBIC contrast in samples subjected to slow cooling,⁵⁴ which had similar effects to low temperature annealing. Also, we note that our findings differ from those of Rinio *et al.* who only found low temperature annealing to have an effect on deteriorated wafers from near the crucible walls and from the bottom of the ingot.³² This difference is probably principally because experiments by Rinio *et al.* were performed after phosphorus diffusion during which the relatively low concentration of bulk impurities in middle wafers are getterted to the emitter.

In general, whilst we have demonstrated that mc-Si can be improved substantially by low temperature annealing, it is perhaps surprising that the improvement is not even greater. The steady state interstitial iron concentrations after the maximum

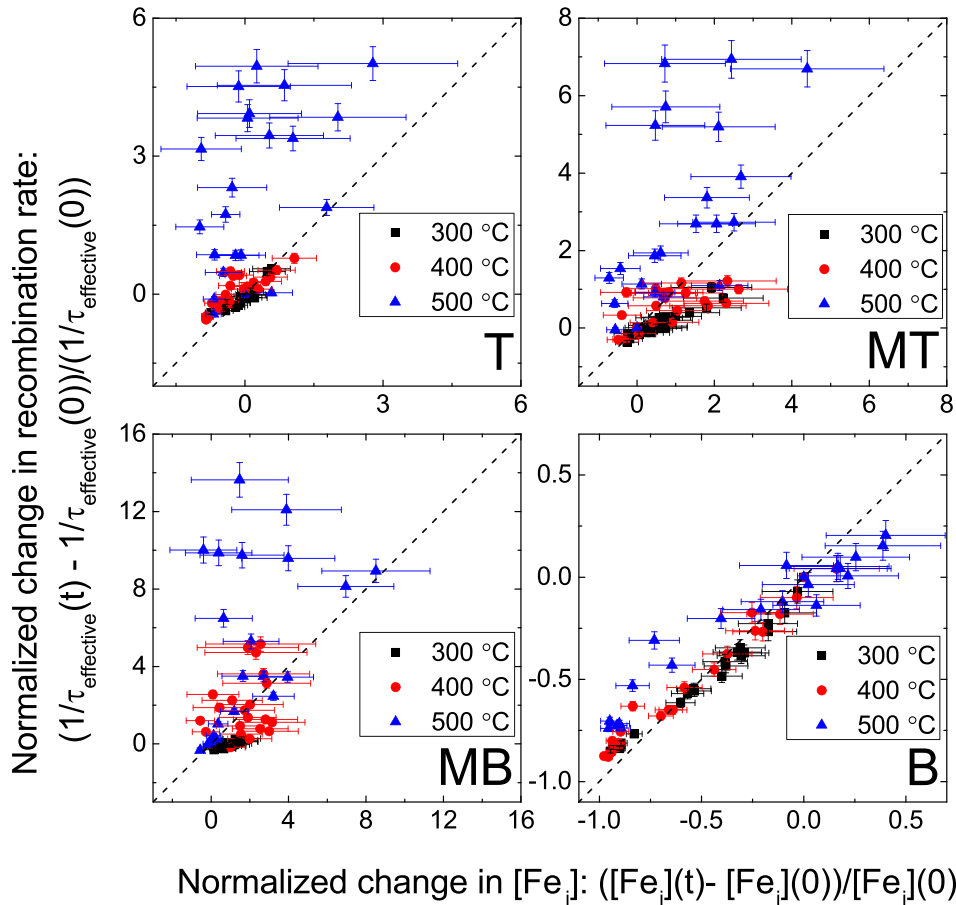


FIG. 10. Change in recombination rate normalized by as-grown recombination rate versus change in bulk iron concentration normalized by as-grown bulk iron concentration according to Equation (1) for samples from the top (T), top middle (MT), bottom middle (MB), and bottom (B) of the mc-Si block. The dashed lines represent a 1:1 relationship.

annealing time (given in Table I) are orders of magnitude higher than extrapolations of the solubility data with respect to an iron silicide phase.^{33,34,56} It is surprising that this remaining supersaturated interstitial iron is not gettered to iron-containing precipitates, or that new precipitates are not nucleated. Understanding why this interstitial iron is apparently trapped in the bulk is an important topic for future study.

D. Kinetics of interstitial iron concentration reduction

The interstitial iron concentration in samples from most of the block did not behave as might be expected from the studies of Krain *et al.*,²⁴ and Liu and Macdonald²⁶ which found the interstitial iron concentration generally to reduce. However, samples from the bottom of the wafer did show a reduction in interstitial iron concentration. An approximately exponential decay in interstitial iron concentration can be parameterised using

$$[Fe_i](t) = [Fe_i](t_{max}) + ([Fe_i](0) - [Fe_i](t_{max}))\exp\left(-\frac{t}{\tau_{decay}}\right) \quad (2)$$

where $[Fe_i](t)$ is the iron concentration after cumulative annealing time t , $[Fe_i](t_{max})$ is the steady-state iron concentration reached after the maximum cumulative annealing time, $[Fe_i](0)$ is the starting interstitial iron concentration, and τ_{decay} is the time constant for the decay in interstitial iron concentration. Overlooking any initial iron increases, fitting

the bottom data in Figure 7 gives τ_{decay} values of 14 h at 300 °C, 4.0 h at 400 °C, and 45 h at 500 °C.

Krain *et al.* found the iron reduction to be dependent on annealing temperature in a way consistent with the temperature dependence of the diffusion coefficient of interstitial iron.²⁴ Given an activation energy for diffusion of 0.67 eV,⁵⁶ the diffusivities at 400 °C and 500 °C are, respectively, expected to be ~ 7.5 times and ~ 33 times higher than at 300 °C. Our values of τ_{decay} are ~ 3.5 times smaller at 400 °C than at 300 °C, and ~ 3.2 larger at 500 °C than at 300 °C. Our results in bottom samples are therefore not consistent with the interstitial iron reduction process being controlled only by diffusion of interstitial iron. In samples from other locations, the relationship is even less clear.

Liu and Macdonald also fitted time constants to their interstitial iron decay data, which like our study was performed using sister wafers.²⁶ For their samples with a starting interstitial iron concentration of $3 \times 10^{12} \text{ cm}^{-3}$ (similar to our bottom samples but taken from a similar block position to our bottom middle samples) they found values of τ_{decay} of ~ 20 h at 400 °C, ~ 6.2 h at 500 °C, ~ 7.6 h at 600 °C, and ~ 50.2 h at 700 °C. The absolute values of time constant cannot be compared between our works, due to different microstructures. However, it is noted that Liu and Macdonald also found the rate of iron decay initially to increase with increasing temperature, then to slow down as temperature increased further. The reduction in rate with increasing temperature is presumably because the supersaturation level is reduced so there is a lower driving force for the formation of new iron-containing precipitates. This could explain our data in bottom samples too.

Two key differences between our methodology and that used by Krain *et al.* may account for the substantial differences between our results. First, they used silicon nitride passivation, which is thought by some to introduce hydrogen into the bulk of the material. A study by Karzel *et al.* compared the effects of a temporary liquid surface passivation scheme (similar, but not identical, to ours) with silicon nitride surface passivation, and found that iron diffusion was affected by the presence of hydrogen from the silicon nitride.³⁵ Liu and Macdonald found a strong dependence on iron precipitation rate on surface passivation type which they attribute to hydrogen incorporation.²⁶ Second, Krain *et al.* state their samples came from different parts of the ingot.²⁴ We have shown that the location within the ingot makes a substantial difference to the behaviour of the interstitial iron concentration (Figure 7), due to substantially different microstructures at the different ingot positions (Figures 4 and 5). It is therefore very difficult to assess the impact of microstructure in their work. In summary, our work and that of Liu and Macdonald²⁶ show that low temperature internal gettering of interstitial iron is significantly more complicated than the diffusion-limited model Krain *et al.*²⁴ As well as diffusion, the concentration of bulk interstitial iron is influenced by the release of interstitial iron into, and capture of interstitial out of, the bulk. We are currently performing additional experiments to assess the role of hydrogen in the process.

V. CONCLUSIONS

We have performed a comprehensive study into the effect of low temperature (300 °C to 500 °C) annealing on lifetime and interstitial iron concentration in as-grown mc-Si. Sister wafers were sourced from four different height positions with differing microstructures characterised by their dislocation distributions. A temporary liquid iodine-ethanol room temperature passivation scheme was used to minimise unintentional hydrogenation and any thermal effects due to the passivation process, so we believe our data show the effect of thermal processing only.

Relatively poor samples from the bottom of the block were improved substantially, and the improvement in lifetime correlated with reductions in interstitial iron concentration. The best results were achieved at 400 °C, at which lifetime was increased from 5.5 μs to 38.7 μs by annealing for ~35 h. Smaller improvements were also realised in top wafers, with lifetime increasing from 12.1 μs to 23.8 μs under the same conditions. The smaller improvement in top wafers is attributed to the higher concentration of recombination-active dislocations. The benefit of low temperature annealing on good wafers from the middle of the block was found to be marginal, with substantial reductions in lifetime initially occurring at 400 °C and 500 °C, followed by a slow recovery.

Our work shows that the effect of low temperature annealing on interstitial iron concentration is much more complicated than found in previous work by Krain *et al.* using silicon nitride passivated samples.²⁴ Annealing at 300 °C to 500 °C was found initially to release interstitial iron into the bulk in many cases, despite the interstitial iron being well above the solubility limit. When the interstitial

iron concentration does decay, its rate is not determined only by the diffusion of interstitial iron. The lack of correlation with interstitial iron in some cases shows that other defects can also play a role during low temperature processing.

In summary, we have demonstrated that low temperature annealing improves the lifetime in certain types of mc-Si used in photovoltaics. It has the potential to be a relatively low cost process for improving red zone wafers, thus enabling the use of more contaminated feedstocks and reducing wastage. Although the annealing times required are fairly long, the conditions required are not dissimilar to those used in the production of some commodity glass products. The key to successful implementation is adding the low temperature gettering at the correct stage in the production process, as junction formation, surface passivation, and firing steps^{32,53,61} all affect the distribution of metallic impurities.

ACKNOWLEDGMENTS

This work was supported by grants from EPSRC (EP/J01768X/2 and EP/M024911/1) and from the Royal Society (RG100076). J.D.M. was supported by a Royal Academy of Engineering/EPSRC Research Fellowship. The authors are grateful to Professor Peter Wilshaw (University of Oxford) for helpful discussions, and also to David Berney Needleman (Massachusetts Institute of Technology) for his assistance with implementation of the dislocation counting algorithm. Data published in this article can be freely downloaded from <http://wrap.warwick.ac.uk/79577/>.

- ¹T. Buonassisi, A. A. Istratov, M. D. Pickett, M. Heuer, J. P. Kalejs, G. Hahn, M. A. Marcus, B. Lai, Z. Cai, S. M. Heald, T. F. Ciszek, R. F. Clark, D. W. Cunningham, A. M. Gabor, R. Jonczyk, S. Narayanan, E. Sauar, and E. R. Weber, "Chemical natures and distributions of metal impurities in multicrystalline silicon materials," *Prog. Photovoltaics: Res. Appl.* **14**, 513 (2006).
- ²I. Takahashi, N. Usami, H. Mizuseki, Y. Kawazoe, G. Stokkan, and K. Nakajima, "Impact of type of crystal defects in multicrystalline Si on electrical properties and interaction with impurities," *J. Appl. Phys.* **109**, 033504 (2011).
- ³A. R. Peaker, V. P. Markevich, B. Hamilton, G. Parada, A. Dudas, A. Pap, E. Don, B. Lim, J. Schmidt, L. Yu, Y. Yoon, and G. Rozgonyi, "Recombination via point defects and their complexes in solar silicon," *Phys. Status Solidi A* **209**, 1884 (2012).
- ⁴S. Pizzini, "Towards solar grade silicon: Challenges and benefits for low cost photovoltaics," *Sol. Energy Mater. Sol. Cells* **94**, 1528 (2010).
- ⁵B. Ziebarth, M. Mrovec, C. Elsässer, and P. Gumbsch, "Interstitial iron impurities at grain boundaries in silicon: A first-principles study," *Phys. Rev. B* **91**, 035309 (2015).
- ⁶B. Ziebarth, M. Mrovec, C. Elsässer, and P. Gumbsch, "Interstitial iron impurities at cores of dissociated dislocations in silicon," *Phys. Rev. B* **92**, 195308 (2015).
- ⁷M. Seibt, V. Kveder, W. Schröter, and O. Voß, "Structural and electrical properties of metal impurities at dislocations in silicon," *Phys. Status Solidi A* **202**, 911 (2005).
- ⁸M. I. Bertoni, D. P. Fenning, M. Rinio, V. Rose, M. Holt, J. Maser, and T. Buonassisi, "Nanoprobe X-ray fluorescence characterization of defects in large-area solar cells," *Energy Environ. Sci.* **4**, 4252 (2011).
- ⁹K. Bothe, R. Krain, R. Falster, and R. Sinton, "Determination of the bulk lifetime of bare multicrystalline silicon wafers," *Prog. Photovoltaics: Res. Appl.* **18**, 204 (2010).
- ¹⁰E. Olsen and E. J. Øvrelied, "Silicon nitride coating and crucible—effects of using upgraded materials in the casting of multicrystalline silicon ingots," *Prog. Photovoltaics: Res. Appl.* **16**, 93 (2008).
- ¹¹G. Stokkan, "Relationship between dislocation density and nucleation of multicrystalline silicon," *Acta Mater.* **58**, 3223 (2010).

- ¹²B. Ryningen, G. Stokkan, M. Kivambe, T. Ervik, and O. Lohne, "Growth of dislocation clusters during directional solidification of multicrystalline silicon ingots," *Acta Mater.* **59**, 7703 (2011).
- ¹³R. Kvande, L. J. Geerligs, G. Coletti, L. Arnberg, M. Di Sabatino, E. J. Øvreliid, and C. C. Swanson, "Distribution of iron in multicrystalline silicon ingots," *J. Appl. Phys.* **104**, 064905 (2008).
- ¹⁴D. Macdonald, A. Cuevas, A. Kinomura, Y. Nakano, and L. J. Geerligs, "Transition-metal profiles in a multicrystalline silicon ingot," *J. Appl. Phys.* **97**, 033523 (2005).
- ¹⁵T. U. Nærland, L. Arnberg, and A. Holt, "Origin of the low carrier lifetime edge zone in multicrystalline PV silicon," *Prog. Photovoltaics: Res. Appl.* **17**, 289 (2009).
- ¹⁶A. A. Istratov, T. Buonassisi, R. J. McDonald, A. R. Smith, R. Schindler, J. A. Rand, J. P. Kalejs, and E. R. Weber, "Metal content of multicrystalline silicon for solar cells and its impact on minority carrier diffusion length," *J. Appl. Phys.* **94**, 6552 (2003).
- ¹⁷A. E. Morishige, H. S. Laine, J. Schön, A. Haarahlitunen, J. Hofstetter, C. del Cañizo, M. C. Schubert, H. Savin, and T. Buonassisi, "Building intuition of iron evolution during solar cell processing through analysis of different process models," *Appl. Phys. A* **120**, 1357 (2015).
- ¹⁸I. Périchaud, "Gettering of impurities in solar silicon," *Sol. Energy Mater. Sol. Cells* **72**, 315 (2002).
- ¹⁹D. Abdelbarey, V. Kveder, W. Schröter, and M. Seibt, "Aluminum gettering of iron in silicon as a problem of the ternary phase diagram," *Appl. Phys. Lett.* **94**, 061912 (2009).
- ²⁰S. P. Phang and D. Macdonald, "Direct comparison of boron, phosphorus, and aluminum gettering of iron in crystalline silicon," *J. Appl. Phys.* **109**, 073521 (2011).
- ²¹H. Talvitie, V. Vähäniemi, A. Haarahlitunen, M. Yli-Koski, and H. Savin, "Phosphorus and boron diffusion gettering of iron in monocrystalline silicon," *J. Appl. Phys.* **109**, 093505 (2011).
- ²²G. Martins, R. S. Bonilla, T. Burton, P. MacDonald, and P. R. Wilshaw, "Minority carrier lifetime improvement of multicrystalline silicon using combined saw damage gettering and emitter formation," *Solid State Phenom.* **242**, 126 (2015).
- ²³J. Hofstetter, D. P. Fenning, D. M. Powell, A. E. Morishige, H. Wagner, and T. Buonassisi, "Sorting metrics for customized phosphorus diffusion gettering," *IEEE J. Photovoltaics* **4**, 1421 (2014).
- ²⁴R. Krain, S. Herlufsen, and J. Schmidt, "Internal gettering of iron in multicrystalline silicon at low temperature," *Appl. Phys. Lett.* **93**, 152108 (2008).
- ²⁵A. Liu, D. Walter, S. P. Phang, and D. Macdonald, "Investigating internal gettering of iron at grain boundaries in multicrystalline silicon via photoluminescence imaging," *IEEE J. Photovoltaics* **2**, 479 (2012).
- ²⁶A. Y. Liu and D. Macdonald, "Precipitation of iron in multicrystalline silicon during annealing," *J. Appl. Phys.* **115**, 114901 (2014).
- ²⁷Y. Boufrad, A. Haarahlitunen, H. Savin, E. J. Øvreliid, and L. Arnberg, "Enhanced performance in the deteriorated area of multicrystalline silicon wafers by internal gettering," *Prog. Photovoltaics: Res. Appl.* **23**, 30 (2015).
- ²⁸R. Falster, "Process for contamination removal and minority carrier lifetime improvement in silicon," U.S. patent No 5,272,119 (1993).
- ²⁹K. J. Fraser, R. J. Falster, and P. R. Wilshaw, "Cathodoluminescence assessment of annealed silicon and a novel technique for estimating minority carrier lifetime in silicon," *Mater. Sci. Eng. B* **159–160**, 194 (2009).
- ³⁰M. D. Pickett and T. Buonassisi, "Iron point defect reduction in multicrystalline silicon solar cells," *Appl. Phys. Lett.* **92**, 122103 (2008).
- ³¹M. Rinio, A. Yodyungyong, S. Keipert-Colberg, Y. P. B. Mouafi, D. Borchert, and A. Montesdeoca-Santana, "Improvement of multicrystalline silicon solar cells by a low temperature anneal after emitter diffusion," *Prog. Photovoltaics: Res. Appl.* **19**, 165 (2011).
- ³²M. Rinio, A. Yodyungyong, S. Keipert-Colberg, D. Borchert, and A. Montesdeoca-Santana, "Recombination in ingot cast silicon solar cells," *Phys. Status Solidi A* **208**, 760 (2011).
- ³³J. D. Murphy and R. J. Falster, "Contamination of silicon by iron at temperatures below 800 °C," *Phys. Status Solidi Rapid Res. Lett.* **5**, 370 (2011).
- ³⁴J. D. Murphy and R. J. Falster, "The relaxation behaviour of supersaturated iron in single-crystal silicon at 500 to 750 °C," *J. Appl. Phys.* **112**, 113506 (2012).
- ³⁵P. Karzel, P. Frey, S. Fritz, and G. Hahn, "Influence of hydrogen on interstitial iron concentration in multicrystalline silicon during annealing steps," *J. Appl. Phys.* **113**, 114903 (2013).
- ³⁶G. Hahn, M. Käs, and B. Herzog, "Hydrogenation in crystalline silicon materials for photovoltaic application," *Solid State Phenom.* **156–158**, 343 (2010).
- ³⁷A. Liu, C. Sun, and D. Macdonald, "Hydrogen passivation of interstitial iron in boron-doped multicrystalline silicon during annealing," *J. Appl. Phys.* **116**, 194902 (2014).
- ³⁸P. Hamer, B. Hallam, S. Wenham, and M. Abbott, "Manipulation of hydrogen charge states for passivation of P-type wafers in photovoltaics," *IEEE J. Photovoltaics* **4**, 1252 (2014).
- ³⁹S. Leonard, V. P. Markevich, A. R. Peaker, B. Hamilton, and J. D. Murphy, "Evidence for an iron-hydrogen complex in p-type silicon," *Appl. Phys. Lett.* **107**, 032103 (2015).
- ⁴⁰T. Buonassisi, A. A. Istratov, S. Peters, C. Ballif, J. Isenberg, S. Riepe, W. Warta, R. Schindler, G. Willeke, Z. Cai, B. Lai, and E. R. Weber, "Impact of metal silicide precipitate dissolution during rapid thermal processing of multicrystalline silicon solar cells," *Appl. Phys. Lett.* **87**, 121918 (2005).
- ⁴¹N. Batra, Vandana, S. Kumar, M. Sharma, S. K. Srivastava, P. Sharma, and P. K. Singh, "A comparative study of silicon surface passivation using ethanolic iodine and bromine solutions," *Sol. Energy Mater. Sol. Cells* **100**, 43 (2012).
- ⁴²R. A. Sinton and A. Cuevas, "Contactless determination of current-voltage characteristics and minority-carrier lifetimes in semiconductors from quasi-steady-state photoconductance data," *Appl. Phys. Lett.* **69**, 2510 (1996).
- ⁴³J. D. Murphy, K. Bothe, M. Olmo, V. V. Voronkov, and R. J. Falster, "The effect of oxide precipitates on minority carrier lifetime in p-type silicon," *J. Appl. Phys.* **110**, 053713 (2011).
- ⁴⁴S. Rein and S. W. Glunz, "Electronic properties of interstitial iron and iron-boron pairs determined by means of advanced lifetime spectroscopy," *J. Appl. Phys.* **98**, 113711 (2005).
- ⁴⁵D. H. Macdonald, L. J. Geerligs, and A. Azzizi, "Iron detection in crystalline silicon by carrier lifetime measurements for arbitrary injection and doping," *J. Appl. Phys.* **95**, 1021 (2004).
- ⁴⁶D. Macdonald and A. Cuevas, "Trapping of minority carriers in multicrystalline silicon," *Appl. Phys. Lett.* **74**, 1710 (1999).
- ⁴⁷A. L. Blum, J. S. Swirhun, R. A. Sinton, F. Yan, S. Herasimenka, T. Roth, K. Lauer, J. Haunschild, B. Lim, K. Bothe, Z. Hameiri, B. Seipel, R. Xiong, M. Dhamrin, and J. D. Murphy, "Inter-laboratory study of eddy-current measurement of excess-carrier recombination lifetime," *IEEE J. Photovoltaics* **4**, 525 (2014).
- ⁴⁸T. Trupke, R. A. Bards, M. C. Schubert, and W. Warta, "Photoluminescence imaging of silicon wafers," *Appl. Phys. Lett.* **89**, 044107 (2006).
- ⁴⁹D. Macdonald, J. Tan, and T. Trupke, "Imaging interstitial iron concentrations in boron-doped crystalline silicon using photoluminescence," *J. Appl. Phys.* **103**, 073710 (2008).
- ⁵⁰W. Wijaranakula, "The reaction kinetics of iron-boron pair formation and dissociation in p-type silicon," *J. Electrochem. Soc.* **140**, 275 (1993).
- ⁵¹B. L. Sopori, "A new defect etch for polycrystalline silicon," *J. Electrochem. Soc.* **131**, 667 (1984).
- ⁵²D. B. Needelman, H. Choi, D. M. Powell, and T. Buonassisi, "Rapid dislocation-density mapping of as-cut crystalline silicon wafers," *Phys. Status Solidi Rapid Res. Lett.* **7**, 1041 (2013).
- ⁵³A. Bentzen, A. Holt, R. Kopecek, G. Stokkan, J. S. Christensen, and B. G. Svensson, "Gettering of transition metal impurities during phosphorus emitter diffusion in multicrystalline silicon solar cell processing," *J. Appl. Phys.* **99**, 093509 (2006).
- ⁵⁴J. Chen, D. Yang, Z. Xi, and T. Sekiguchi, "Recombination activity of Σ3 boundaries in boron-doped multicrystalline silicon: Influence of iron contamination," *J. Appl. Phys.* **97**, 033701 (2005).
- ⁵⁵T. Buonassisi, A. A. Istratov, M. D. Pickett, M. A. Marcus, T. F. Ciszek, and E. R. Weber, "Metal precipitation at grain boundaries in silicon: Dependence on grain boundary character and dislocation decoration," *Appl. Phys. Lett.* **89**, 042102 (2006).
- ⁵⁶A. A. Istratov, H. Hieslmair, and E. R. Weber, "Iron and its complexes in silicon," *Appl. Phys. A* **69**, 13 (1999).
- ⁵⁷D. P. Fenning, A. S. Zuschlag, M. I. Bertoni, B. Lai, G. Hahn, and T. Buonassisi, "Improved iron gettering of contaminated multicrystalline silicon by high-temperature phosphorus diffusion," *J. Appl. Phys.* **113**, 214504 (2013).
- ⁵⁸P. S. Plekhanov, R. Gafiteanu, U. M. Gösele, and T. Y. Tan, "Modeling of gettering of precipitated impurities from Si for carrier lifetime improvement in solar cell applications," *J. Appl. Phys.* **86**, 2453 (1999).
- ⁵⁹J. D. Murphy, K. Bothe, V. V. Voronkov, and R. J. Falster, "On the mechanism of recombination at oxide precipitates in silicon," *Appl. Phys. Lett.* **102**, 042105 (2013).
- ⁶⁰J. D. Murphy, R. E. McGuire, K. Bothe, V. V. Voronkov, and R. J. Falster, "Competitive gettering of iron in silicon photovoltaics: Oxide precipitates versus phosphorus diffusion," *J. Appl. Phys.* **116**, 053514 (2014).
- ⁶¹J. F. Lelièvre, J. Hofstetter, A. Peral, I. Hoces, F. Recart, and C. del Cañizo, "Dissolution and gettering of iron during contact co-firing," *Energy Proc.* **8**, 257 (2011).